

STATISTICAL PROPERTIES OF MAGNETIC SEPARATORS IN MODEL ACTIVE REGIONS

BRIAN T. WELSCH AND DANA W. LONGCOPE

Montana State University, Bozeman

Received 1998 December 14; accepted 1999 April 19

ABSTRACT

Previous theoretical work suggests that magnetic reconnection in the solar corona should occur along particular topological boundaries in the coronal magnetic field known as separators. Thus, a field's topological structure predicts the locations of X-ray/EUV loops, assuming enhanced emission is related to reconnection. We use this topological model in a theoretical study of the statistical properties of active-region loops. We model the interaction of a single “test” element of photospheric magnetic flux with a much larger distribution of flux of the opposite polarity. We first model the large-scale distribution of flux in an active region using a mean-field approach and develop a procedure to determine separator lengths. We then perform Monte Carlo simulations to check the accuracy of this approximation. The results of both methods are similar and are well described by simple scaling laws for separator lengths. Separator lengths scale as $\sim \exp(\alpha r)/N^{1/2}$, where N parameterizes the flux in the large-scale distribution and r is the distance of the test element from the distribution's center. This scaling law is a theoretical prediction of X-ray loop lengths, which can be compared with observations.

Subject headings: plasmas — Sun: corona — Sun: flares — Sun: magnetic fields

1. INTRODUCTION

1.1. *How Is the Corona Heated?*

Physicists still do not understand the precise mechanism by which the solar corona is heated to a temperature of several million kelvins (MK), 2 orders of magnitude hotter than the chromosphere immediately beneath it. In one picture, energy is dissipated in the corona as a by-product of some process involving the reconnection of magnetic field lines there (Gold 1964; Parker 1983). At present, however, observations do not constrain the myriad theoretical models of reconnection in the corona, where the large length scales and high conductivity mean magnetic field lines are effectively frozen to the plasma.

Nonetheless, detailed observations in X-ray (Lin et al. 1984), H α (Canfield & Metcalf 1987), and simultaneous observations in X-ray and UV (Porter, Fontenella, & Simnett 1995) have shown that aperiodic events on small spatial scales and short timescales regularly deposit $\sim 10^{27}$ ergs of energy in the corona. These observations, consistent with reconnection processes, suggest that small-scale, flare-like events might be heating the corona. Since this energy is $\sim 10^{-6}$ times that seen in large flares, the term “microflares” has been associated with these phenomena.

Short-term heating of X-ray loops, in the form of “transient brightenings,” are also regularly seen in images taken with the soft X-ray telescope (SXT) on board the *Yohkoh* satellite (Shimizu et al. 1992). These events typically last for a few minutes and occur with frequencies ranging from one every few minutes to one per hour, depending on just how “active” the host active region is (Shimizu et al. 1992). Such events are typified by an initial brightening of loop footpoints that leads to brightening of the entire loop, and simultaneous brightenings in multiple loops are not uncommon. For these reasons, Shimizu et al. (1994) attributes these phenomena to “the magnetic interaction of multiple loops.”

Estimates of the energy released in these events, 10^{25} – 10^{29} ergs (Shimizu 1995), are near estimates of the energy released in microflares (Porter et al. 1995), and some (e.g.,

Gary, Hartl, & Shimizu 1997) speculate that these two flare-like phenomena are, in fact, identical.

Nomenclature aside, these events contribute significantly to coronal heating above active regions. While Porter et al. (1995) argues only that microflares “cannot be dismissed” as a component of active-region heating processes, Shimizu (1995) has placed an upper bound on the total energetic contribution of transient brightenings to active-region heating at about 20% of that required to account fully for active-region temperatures.

One puzzling aspect of these phenomena is that the mechanism responsible for the brightenings is quite selective. Because the gas pressure in the tenuous corona is much less than the magnetic pressure there ($\beta \equiv P_{\text{gas}}/P_{\text{magnetic}} \ll 1$), the magnetic field is believed to fill the entire coronal volume. But the coronal plasma is bright in X-rays along only a few of the field lines above an ordinary active region, as may be seen in the example shown in Figure 1.

Where does the energy that is released in these transient brightenings and microflares originate? The structure of the coronal magnetic field is primarily a product of the distribution of the field at the photosphere. Flux elements seen in magnetograms are interpreted as the cross sections of slender flux tubes whose tops have emerged into the corona (Parker 1955; D’Silva & Choudhuri 1993; Fan, Fisher, & McClymont 1994; Caligari, Moreno-Insertis, & Schüssler 1995). Models suggest that, in the low- β plasma above the photosphere, the isolated flux tubes expand to fill space (Gabriel 1976). In one common view of flare energetics, photospheric flows shuffle the locations of these magnetic flux elements. This increases the complexity of the coronal field, gradually increasing the stress and, hence, the energy stored in that field (Gold & Hoyle 1960; Van Hoven et al. 1980). When this energy is suddenly released into the corona, we observe its signature in various ways, most notably in enhanced coronal emission.

Like the energy release in “true” flares, that in microflares is impulsive (Porter et al. 1995), and particles are accelerated with sufficient energy to generate X-rays characteristic of $T \sim 10$ MK plasmas. These qualities suggest that

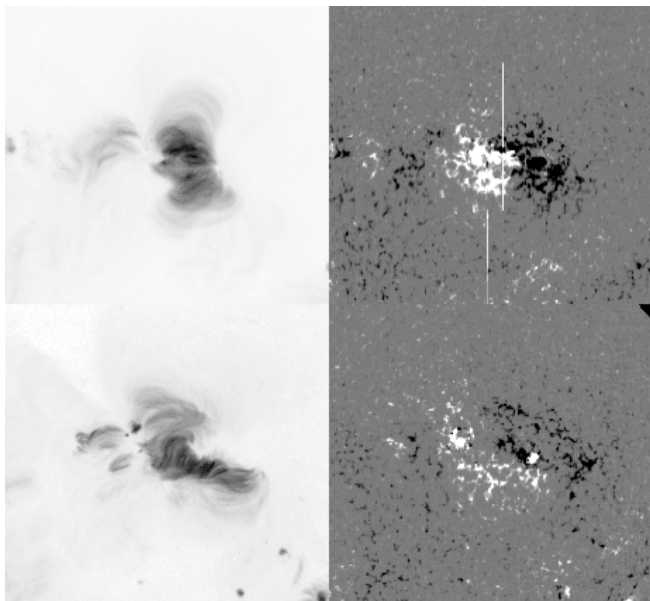


FIG. 1.—Yohkoh SXT images (left) of an active region, juxtaposed with Kitt Peak line-of-sight magnetograms (right) of the same active region, over two successive solar rotations (top row/bottom row, respectively): SXT—1992 July 5, 14:39:44 UT/1992 August 1, 16:58:21 UT; Kitt Peak—1992 July 5, 14:29:17 UT/1992 August 2, 15:07:01 UT. Because the gas pressure is so slight in the tenuous corona ($P_{\text{gas}}/P_{\text{magnetic}} \equiv \beta \ll 1$), magnetic fields above the active region fill all space. Obviously, however, only a few field lines are bright in soft X-rays. Why? (Courtesy of A. Pevtsov).

microflares are indeed members of the “flare family” (Porter et al. 1995). We therefore assume that energy released in microflares and transient brightenings was stored in field stresses before these events.

1.2. Simplifying Assumptions

Since the build-up of stress in the field is typically a rather slow process, the long timescales and small electric fields involved mean the approximations of ideal magnetohydrodynamics (MHD) apply (Longcope 1996).

Two other approximations are adopted solely for simplicity. The first is that the coronal magnetic field is current-free,

$$\nabla \times \mathbf{B} = 0, \quad (1)$$

meaning that it may be represented by the gradient of a scalar potential field,

$$\mathbf{B} = -\nabla\chi. \quad (2)$$

In the second assumption, we take the coronal field to be that which would arise if the flux elements at the photosphere were pointlike “magnetic charges,”

$$\mathbf{B}(\mathbf{x}) = \sum_{i=1}^N \frac{q_i(\mathbf{x} - \mathbf{x}_i)}{|\mathbf{x} - \mathbf{x}_i|^3}, \quad (3)$$

where $\psi_i = 2\pi q_i$ is the flux in footpoint i and \mathbf{x}_i is its location. The field in the corona is then uniquely determined by the solution of Laplace’s equation,

$$\nabla \cdot \mathbf{B} = -\nabla^2\chi = 0, \quad (4)$$

where the distribution of discrete flux elements at the photosphere (for all i , $z'_i = 0$) is imposed as a boundary condition (Longcope & Fisher 1996).

1.3. Magnetic Charge Topology

By grouping field lines according to their endpoints, classes of field lines are delineated by the various possible linkages. In this framework, Sweet (1958) first showed that well-defined boundaries exist between basins of differing connectivity and termed these boundaries *separatrices* and *separators*. Baum & Bratenahl (1980) first quantified the description of the field in topological terms; several authors have since revisited and refined their approach (Gorbachev & Somov 1988; Priest & Forbes 1989; Somov 1992; Lau 1993; Démoulin, Hénoux, & Mandrini 1994; Parnell, Priest, & Golub 1994). Descriptions of magnetic fields in these topological terms have been grouped under the rubric of *magnetic charge topology* (MCT; Longcope 1996).

These topological boundaries are expected to be the sites of reconnection and consequent energy release, seen in the form of flares and microflares (Longcope 1996). The selective brightening mechanism revealed in the images in Figure 1 makes sense in this context: only separator field lines emit in X-rays, because reconnection deposits energy only at or near these field lines.

In this work, we employ the techniques of MCT to make semiempirical predictions of statistical properties of separators as they would occur in solar active regions. This is the first step in a larger calculation, that of coronal heating rates due to reconnection along separators in active regions. In this work, we present the length distribution of separator loops occurring in simple models of active regions. These results can be compared to observations of coronal X-ray loops. Further, we explore dependence of loop lengths on quantities one can assign to every active region, namely, physical size and total flux.

Shimizu et al. (1994) has compiled rough statistics on the lengths of coronal loops observed with SXT. As the first step toward an explanation of his results on the basis of theory alone, this investigation is the first study of its kind. It is also a test of the validity of the MCT model. The work presented here forms the basis of further investigations, already underway, involving more complex models of active regions.

In the next section we describe the separator model in more detail, first defining the topological entities to which the model refers and then briefly discussing role of reconnection in this model. In § 3 we approximate the large-scale fields in active regions with analytic functions, derived from mean-field averaging, and develop a technique for finding separator lengths. This mean-field technique is intuitively clear and promises to be applicable to a wider class of active-region models. In § 4 we use a Monte Carlo method to find separator lengths in model active regions composed of individual flux elements to test the mean-field approach. Finally, in the last section, we compare the results obtained with these two methods and discuss their implications.

2. THE SEPARATOR MODEL

2.1. Charges in a Uniform Field

To introduce the relevant aspects of MCT, we consider a simple charge configuration (after Longcope 1998). Suppose

first that a single magnetic “test” charge $q_B < 0$, labeled N , is situated on a plane photosphere and that it is immersed in a uniform, horizontal background field, B_0 .

An axis of symmetry runs parallel to this background field through the test charge. Along this axis, the total field identically vanishes at a point that is a distance

$$\Delta = \sqrt{\frac{|q_B|}{B_0}} \quad (5)$$

from the test charge, in the direction parallel to the background field. For future reference, this *null point* is labeled A .

Most field lines in this configuration can be grouped into two categories, according to their endpoints: (1) field lines that begin at infinity and end at N , and (2) field lines constituting the background field, which begin at infinity and end at infinity.

Some field lines end at neither N nor infinity and thus fall into a third category: they end at the null, A . These field lines form the boundary surface between the domains of differing connectivity: inside, all field lines end at the test charge; outside, none do. This boundary is the charge’s *separatrix surface*, which we label Σ_A and show in Figure 2a.

A curve is formed by the intersection of the separatrix Σ_A and the photosphere; we call this the “rim” of the separatrix and label it \mathcal{C}_Σ . Tracing the rim will prove useful to the extent that it delineates the field topology above the photosphere (see Figure 2b).

Now suppose we add to this configuration a positive charge, P , equal in magnitude and opposite in sign to N . Barring cases of special symmetry, P has its own null, which we label B , and its own separatrix surface, Σ_B , that encloses its flux. The two magnetic nulls, A and B , have different geometric properties, which we elaborate upon shortly.

If P is “far” from N , Σ_B looks much like Σ_A but differs in orientation: the former opens away from the background field, while the latter opens toward it. “Far,” in this context, means the charges’ separation is much greater than the characteristic length given by equation (5). It can be shown that the “diameter” of each roughly cylindrical separatrix surface is approximately 4 times this length—meaning the two charges’ separatrices do not intersect in this case.

If the separatrices do not intersect, then no field lines have endpoints at both charges, or, equivalently, the two charges do not share flux with each other. In this case, then, the analysis used to describe the field topology in the single-charge case applies equally well to each individual charge.

If, however, the charges are “close” in the same sense as above, then they do share flux with each other (see Figs. 3a and 3b). In this case, there are two additional topological categories of field lines. The first class contains those lines that originate at one charge and end at the other; we denote this shared flux by ψ_{PN} . These field lines, from the very definition of a separatrix, lie within that volume enclosed by both of the charges’ separatrices.

The other class contains only one field line, that formed by the intersection of the two separatrix surfaces; as such, it must begin at the positive charge’s null, B , and end at the negative charge’s null, A . It is called a *separator*, and we label it σ (see Fig. 3c); it encircles all of those field lines that have endpoints at the two charges and no others (Longcope & Cowley 1996).

The final panel in Figure 3 illustrates the separator loop’s significance: it is the three-dimensional analog of an X -point in two dimensions. It has long been known that X -points play significant roles in the reconnection of magnetic fields in two dimensions. The separator plays this role in three dimensions (Greene 1988; Lau & Finn 1990). The remainder of this work will study the properties of separators in model active regions.

2.2. Reconnection along a Separator

Combining a line segment that runs from A to B in the $z = 0$ plane with the separator σ forms a complete loop, labeled \mathcal{C} . The line integral of the magnetic vector potential \mathbf{A} along this loop returns precisely the shared flux,

$$\psi_{PN}^{(v)} = \oint_{\mathcal{C}} \mathbf{A} \cdot d\mathbf{l}, \quad (6)$$

where the direction of the integral is such that the integration proceeds parallel to the magnetic field along σ , and the superscript (v) reminds us that this is the vacuum flux (Longcope 1996).

Suppose displacement of the two charges (due, for instance, to photospheric flows) alters the net vacuum flux that \mathcal{C} encloses by an amount $\Delta\psi_{PN}$. But, as Longcope & Cowley (1996) pointed out, the plasma, assumed a perfect conductor, will not allow any change in flux through \mathcal{C} . Instead, a *current ribbon* instantaneously forms along the separator, with total current I flowing in such a way as to generate a self-flux $\psi^{(cr)}(I)$, which exactly cancels $\Delta\psi_{PN}$ (Longcope & Cowley 1996), viz.,

$$\psi_{PN}^{(v)} + \psi^{(cr)}(I) = \psi_0 + \Delta\psi_{PN}^{(v)} + \psi^{(cr)}(I) = \psi_0. \quad (7)$$

Longcope (1996) found an expression of the energy difference between the current-free field and the field with the current ribbon. This energy arises from the self-inductance of a loop in which a current is first turned on and then ramped up to the value that generates $\psi^{(cr)} = -\Delta\psi_{PN}^{(v)}$. The salient point for this discussion is that this expression for the energy depends strongly upon the current, I , and the separator length, l . The primary results derived here are the statistical properties of the latter, a purely geometric quantity.

If, via some instability, reconnection then occurs along the separator, flux will be transferred across the separator until the field relaxes to a new potential configuration, and the current ribbon will disappear. The excess energy due to the ribbon current will then be liberated, heating the coronal plasma and evaporating chromospheric plasma in the neighborhood of the separator. This, in turn, will be seen as sudden X-ray brightening near the separator (Longcope 1998).

2.3. Properties of Null Points

Near the location of a first-order null, \mathbf{x}_* , the magnetic field can be described by the second term in a Taylor series,

$$\mathbf{B}(\mathbf{x}_* + d\mathbf{x}) = M(\mathbf{x}_*) \cdot d\mathbf{x} + \dots, \quad (8)$$

where the elements of the Jacobian matrix $M(\mathbf{x}_*)$ are $M_{ij} = (\partial B_i / \partial x_j)|_{\mathbf{x}_*}$. Since the field is potential, the matrix is symmetric and thus has three real eigenvalues, and three orthogonal eigenvectors (Longcope 1996). As

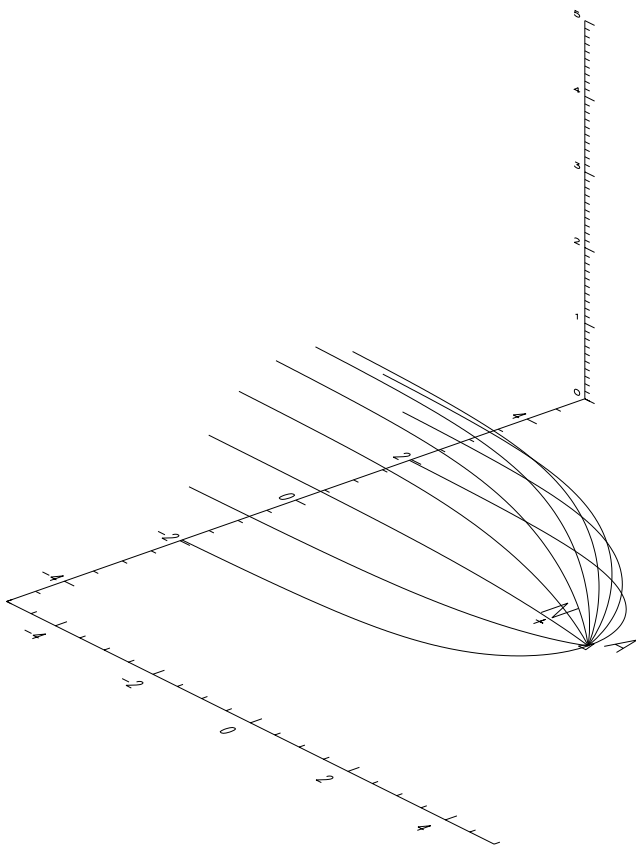


FIG. 2a

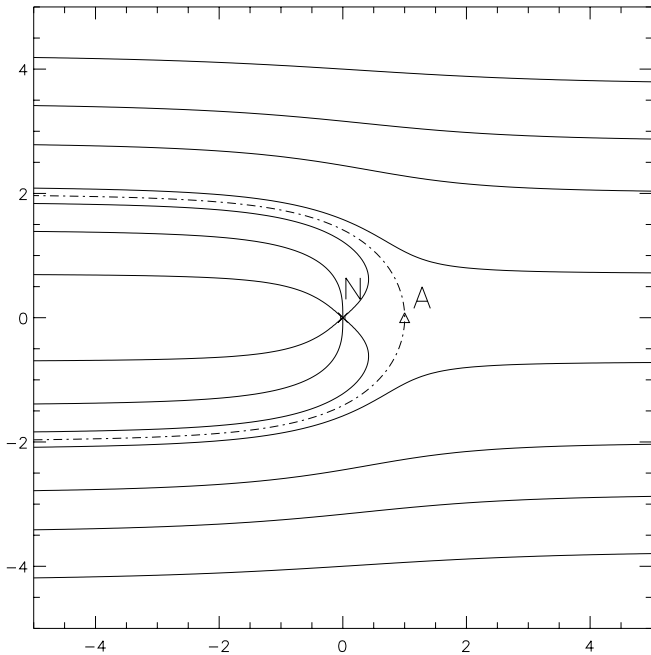


FIG. 2b

FIG. 2.—(a) Separatrix Σ_A encloses the flux N shares with the background field. All field lines on Σ_A end at the null, A . (b) Selected photospheric field lines, including the separatrix “rim,” \mathcal{C}_s , the curve formed by the intersection of the separatrix with the photosphere (dash-dotted line). Note the change in connectivity across \mathcal{C}_s . Axes in both figures are in units of the characteristic length, Δ , from eq. (5).

$\nabla \cdot B = \text{Tr}(M) = 0$, two eigenvalues must differ in sign (Cowley 1973; Yeh 1976), and the sign of the third delineates two classes of nulls (Cowley 1973): *A*-type nulls have two negative eigenvalues, and *B*-type nulls have two positive eigenvalues. The terms *negative* and *positive* nulls, respectively, have also been used (Priest & Forbes 1999; Priest & Titov 1996).

This delineation of two classes of nulls, based upon the sign of the intermediate eigenvalue of the Jacobian matrix, neglects the possibility that this eigenvalue may vanish. The null in such a case is not *generic*; we digress to discuss briefly this eventuality. Consider a null in some configuration in which the intermediate eigenvalue of the Jacobian, though small, is nonzero. By changing the amplitude or location of a charge near the null, both the null’s location and its Jacobian are perturbed. When the intermediate eigenvalue is sufficiently small, such a perturbation can change the sign of the eigenvalue. Such events occur and are significant in later numerical simulations. In particular, when a null at the photosphere undergoes such a “pitchfork” bifurcation, the null changes type, and two additional nulls of the same type as the original appear above and below the photosphere. (For more on such bifurcations, see, e.g., Priest, Lonie, & Titov 1996.) As the properties of such configurations are beyond the scope of the current theory, only generic cases (without bifurcations) are considered in what follows.

In general, field lines leave an *A*-type null along two lines that run in opposite directions along the eigenvector corresponding to the null’s sole positive eigenvalue. These are the null’s “spines” (Priest & Titov 1996) or “ γ -lines” (Lau & Finn 1990). For an *A*-type null, they run from the null to two negative charges. An *A*-type null is therefore associated with negative charges; hence the term “negative null.”

Locally, field lines enter an *A*-type null within the two-dimensional surface spanned by the two negative eigenvectors, forming a so-called fan-plane (Priest & Titov 1996). Further from the null, the macroscopic field deforms this flat plane into a curved surface—the separatrix. The geometry near a *B*-type null is analogous, with all directions reversed.

Field lines on a given side of the separatrix surface have an endpoint at the same charge that the spine on that side of the surface does. This means that the separatrix forms the boundary between field lines having different connectivity. Hence, as mentioned above, a given charge’s separatrix demarcates the volume that contains all of that charge’s flux.

In a configuration with multiple charges and only generic, first-order nulls (i.e., barring cases of special symmetry, or cases where bifurcations have occurred), one can argue that the number of nulls is one fewer than the number of charges. The presence of an “orphan” charge notwithstanding, however, it is in principle possible to associate a particular null with each charge, and vice versa. To understand this, imagine that a charge is added to a preexisting configuration of charges by being “turned on,” its amplitude raised from zero in small steps. The instant the charge appears, a null also appears, quite near the charge, and the two are easily associated by their proximity. (Their separation is given by equation [5], where B_0 is the strength of the field before the charge is turned on.) As the charge’s amplitude is increased further, however, the null-charge separation increases, and variations in the background field have

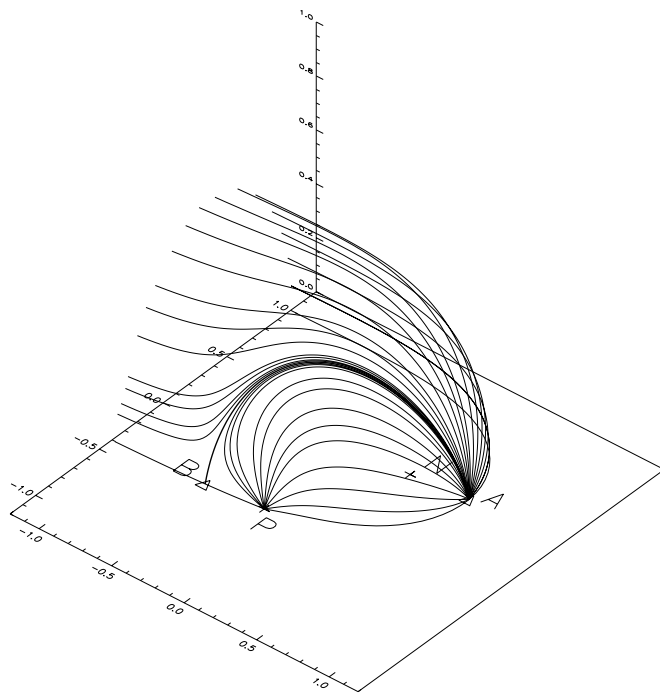


FIG. 3a

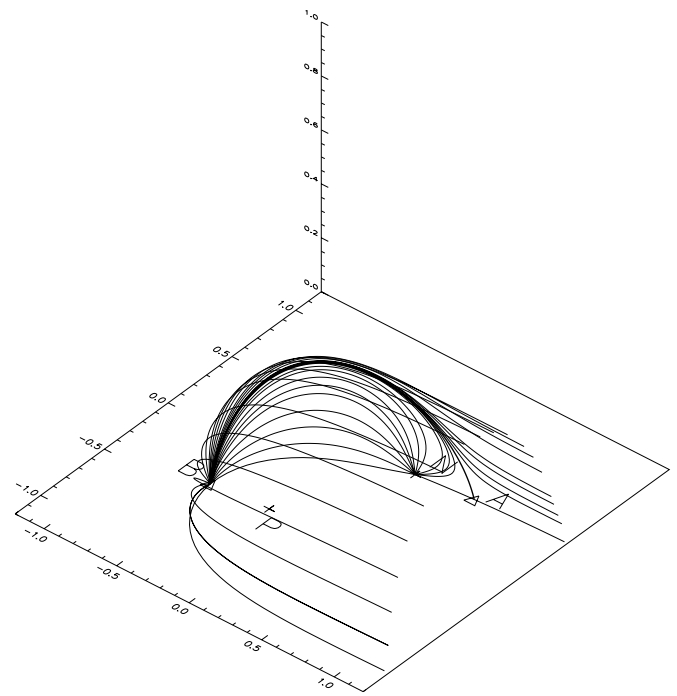


FIG. 3b

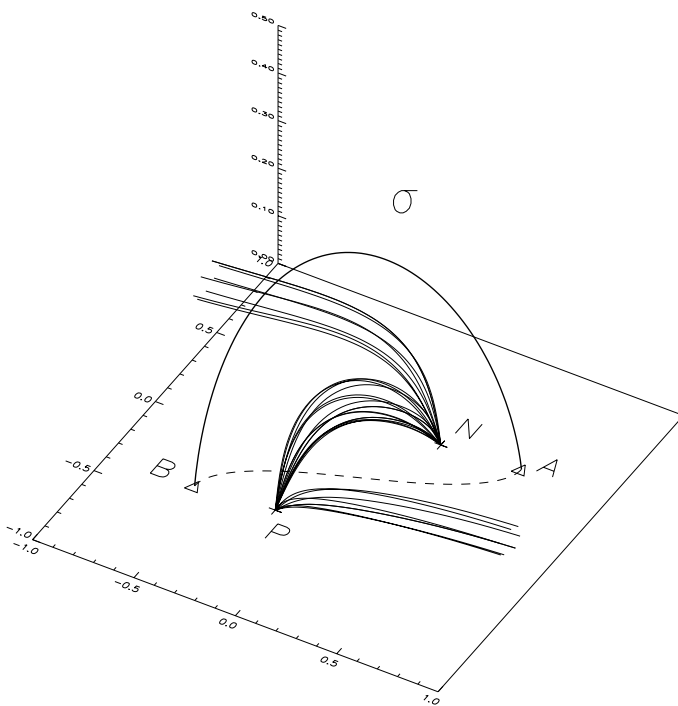


FIG. 3c

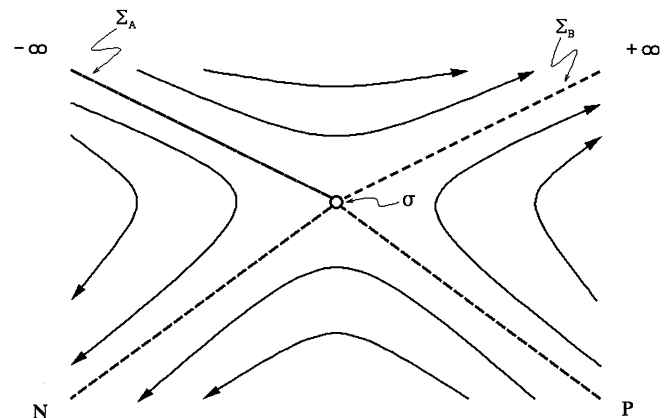


FIG. 3d

FIG. 3.—(a) Separatrix Σ_A encloses the flux N shares with the background field and P . (b) The separatrix Σ_B encloses the flux P shares with the background field and N . (c) The intersection of Σ_A with Σ_B forms the separator loop, σ . The only field line on both separatrices, it must begin at the positive null, B , and end at the negative null, A . Here a selection of the bipole's field lines is shown, along with some of the lines that connect each charge to the background field. (d) A schematic of field line topology in a cross section perpendicular to the separator, σ , showing X-type field geometry along separator. (The first three figures are taken from Longcope 1998.)

complex effects upon the “motion” of the null away from “its” charge. Consequently, in practice, it is nontrivial to find the null associated with a particular charge in a given configuration. Nevertheless, we will often use the conceptual connection between charges and nulls.

3. MEAN-FIELD MODELS OF ACTIVE REGIONS

Solar active regions are composed of many individual flux elements, which can be modeled as magnetic charges of varying strengths (Longcope 1996). To model the properties of large collections of such charges more easily, we special-

ize to the case of charge distributions composed of N small flux elements, all of the same flux. The field is then given by equation (3), with each q_i replaced by the same constant, q_0 .

Such a configuration is a rudimentary model of one polarity of a bipolar active region whose total flux is $q_0 N = 10^{21}$ Mx, where $q_0 \approx 10^{19}$ Mx, and the number of elements N is on the order of 100. In a typical such active region, the elements would be distributed within an area measuring tens of Mm in diameter.

We assume the magnetic flux elements in a large region of concentrated magnetic flux will diffuse by a random walk, owing to turbulent photospheric motions (Leighton 1964; see also Fig. 1). Thus, it is appropriate to model the probability distribution function describing the flux elements' locations (x'_i, y'_i) as Gaussian,

$$p(x'_i, y'_i) = \frac{1}{2\pi\delta^2} \exp \left\{ -\frac{[(x'_i)^2 + (y'_i)^2]}{2\delta^2} \right\}, \quad (9)$$

where δ is the width of this distribution. We use coordinates scaled to δ , with the origin located at the distribution's centroid.

3.1. Field Averaging

When N is large, using equation (3) to find nulls and topologically important field lines is feasible only with numerical methods. We expect, however, that expressions for ensemble-averaged quantities could be more easily attacked with analytic methods. Accordingly, we now consider such averages.

To simplify our task, we assume that the field topology above the photosphere is determined by the separatrix rim at the photosphere (see Fig. 2b), meaning that we need only consider expressions for the field at $z = 0$.

In Appendix A, we find the average vertical field at the photosphere to be given by

$$\bar{B}_z(r) = \frac{q_0 N}{\delta^2} e^{-r^2/2\delta^2}, \quad (10)$$

where $r^2 = x^2 + y^2$. Hence, the average vertical field, like the probability distribution function of charge locations, is Gaussian.

In Appendix B, we then find the average radial field at the photosphere to be given by

$$\begin{aligned} \bar{B}_r(r, 0) &= \sqrt{\frac{\pi}{2^3}} \frac{q_0 N}{\delta^2} \left(\frac{r}{\delta} \right) \exp \left(\frac{-r^2}{4\delta^2} \right) \\ &\times \left[I_0 \left(\frac{r^2}{4\delta^2} \right) - I_1 \left(\frac{r^2}{4\delta^2} \right) \right], \end{aligned} \quad (11)$$

where I_0 and I_1 are modified Bessel functions.

3.2. Methods

We now consider a “test” charge, immersed in the non-uniform mean field arising from a Gaussian collection of “field” charges. For a separator to exist, the test charge must share flux with this background field, meaning that it must differ in sign from the background field.

The primary result sought is the probability distribution of separator lengths, as a function of both the location of the test charge, and the net flux in the background field. We proceed under two assumptions:

1. The probability that a separator connects the test charge's null with a field charge's null is directly related to the probability that the test charge shares flux with a field charge.

2. The probability that the test charge shares flux with a field charge is proportional to the average vertical flux \bar{B}_z contained within the separatrix rim \mathcal{C}_Σ , the intersection of the test charge's separatrix with the photosphere.

We adopt the first assumption because the existence of separatrices is a necessary condition for the existence of a separator. We embrace the second because the average vertical field's distribution is identical to the field charges' spatial probability distribution; hence, “more average vertical field enclosed” amounts to “more probability of enclosing a field charge.”

To find the flux enclosed by the separatrix rim, we must first find the two field lines that form \mathcal{C}_Σ . The horizontal field at the photosphere combines the field of the test charge, located at $(x_0, 0, 0)^T$, and that of the Gaussian distribution of field charges,

$$\begin{aligned} B_x(x, y) &= \left(\frac{x}{\sqrt{x^2 + y^2}} \right) \bar{B}_r(\sqrt{x^2 + y^2}) \\ &+ \frac{(x - x_0)}{|(x - x_0)^2 + y^2|^{3/2}} \end{aligned} \quad (12)$$

$$\begin{aligned} B_y(x, y) &= \left(\frac{y}{\sqrt{x^2 + y^2}} \right) \bar{B}_r(\sqrt{x^2 + y^2}) \\ &+ \frac{(y)}{|(x - x_0)^2 + y^2|^{3/2}}. \end{aligned} \quad (13)$$

Here we have assumed that the test charge is of unit strength; by varying the parameter N appearing in equation (11), we can change the strength of the background field.

3.3. Tracing the Separatrix Rim

The separatrix surface follows field lines that end at the A -type null associated with the test charge. These field lines enter the null along the surface defined by the negative eigenvectors of the null's Jacobian matrix, \mathbf{M} . The separatrix rim \mathcal{C}_Σ will follow that eigenvector parallel to the photosphere. We trace the rim in each direction leaving the null, by integrating the field line equation numerically. Figure 4a shows the separatrix rim of a test charge located at $r = 1.5$.

In the mean-field approximation, all the flux that connects to the test charge will originate from within the curve \mathcal{C}_Σ .

We define $Q_{\text{enc}}(R)$ to be the normal flux enclosed by \mathcal{C}_Σ within a distance R of the test charge. To find $Q_{\text{enc}}(R)$, we integrate \bar{B}_z in annular rings, centered at the test charge, increasing the radius R at each step. To ensure smoothness in $Q_{\text{enc}}(R)$, we take 50 incremental steps in R .

These ideas are illustrated in Figure 4b for the case of a test charge on the tail of a distribution, at $r_{\text{test}} = 1.5$ from the distribution's centroid, with $N = 100$.

3.4. Probabilistic Arguments

The function $Q_{\text{enc}}(R)$ can be used to calculate the mean-field approximation to the distribution of separator lengths. We will limit our considerations to the length of the shortest

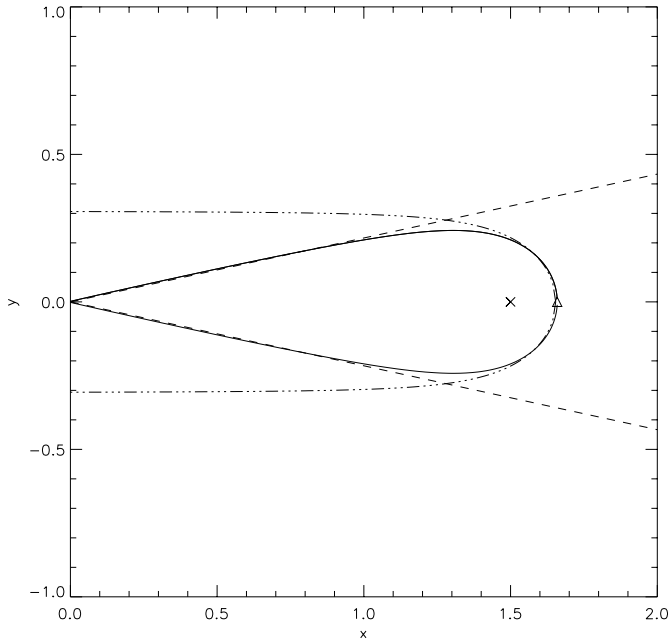


FIG. 4a

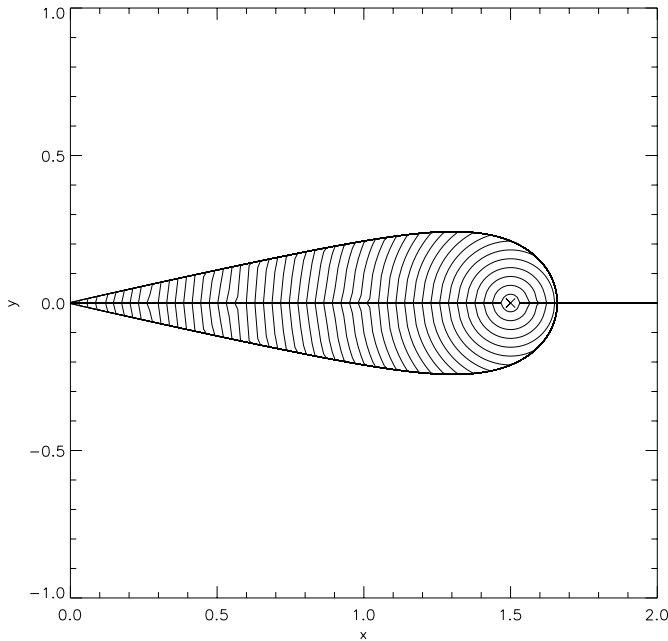


FIG. 4b

FIG. 4.—(a) Separatrix rim, \mathcal{C}_Σ , plotted (solid line) for a background field strength 100 times that of the test charge, which is located at $r_{\text{test}} = 1.5$. Also plotted are the radial asymptotes of the field lines as they near the origin (dashed line) and the separatrix of a test charge in a uniform background field (dash-dotted line) of strength $B_0 = \bar{B}_r(1.5)$. Test charge and null are marked by the cross and the open triangle, respectively. (b) $Q_{\text{enc}}(R)$, the normal flux \bar{B}_z enclosed by the rim, \mathcal{C}_Σ , within a distance R of the test charge, is integrated in annular rings, centered on the test charge, for the same case. Coordinate axes are in units of δ .

separator. Because it has the least inductance, the shortest separator will have the largest current. (Recall that, for fixed flux, current is inversely proportional to self-inductance.) Hence, while photospheric motions alter the flux through all of the configuration's separators, the shortest is the most likely site of transient brightenings.

The probability that the curve \mathcal{C}_Σ does not enclose a single one of the N charges within the radius R is

$$P_0(R) = \left[1 - \frac{Q_{\text{enc}}(R)}{Q_{\text{tot}}} \right]^N, \quad (14)$$

where $Q_{\text{tot}} = q_0 N$ is the total magnetic charge in a distribution of N background charges. The probability of enclosing at least a single charge is therefore

$$P(R) = 1 - P_0(R) = 1 - \left[1 - \frac{Q_{\text{enc}}(R)}{Q_{\text{tot}}} \right]^N. \quad (15)$$

We define the conditional probability $\tilde{P}(R)$, which is the probability of enclosing at least one charge within radius R given that at least one is enclosed within \mathcal{C}_Σ . Using Bayes's theorem (Press et al. 1988), this conditional probability is

$$\begin{aligned} \tilde{P}(R) &\equiv P(R | R_{\text{max}}) = \frac{P(R_{\text{max}} | R)P(R)}{P(R_{\text{max}})} \\ &= \frac{1 - [1 - (Q_{\text{enc}}(R)/Q_{\text{tot}})]^2}{1 - 1 - \{[Q_{\text{enc}}(R_{\text{max}})/Q_{\text{tot}}]\}^2}, \end{aligned} \quad (16)$$

where R_{max} is the point on \mathcal{C}_Σ farthest from the test charge.

The expectation value of a quantity $F(R)$ can be determined from the differential probability distribution,

$$\langle F \rangle = \frac{\int_0^{R_{\text{max}}} dR [d\tilde{P}(R)/dR] F(R)}{\int_0^{R_{\text{max}}} dR [d\tilde{P}(R)/dR]} = \int_0^{R_{\text{max}}} dR \frac{d\tilde{P}(R)}{dR} F(R). \quad (17)$$

Similarly, the standard deviation can be defined

$$\Delta F = \sqrt{\langle F^2 \rangle - \langle F \rangle^2}. \quad (18)$$

Thus, we have a prescription for calculating the expected distance from the test charge to the nearest field charge, $\langle R \rangle$, and its standard deviation ΔR .

In Figure 5 we plot several of the quantities appearing in these calculations for $N = 100$ and $r_{\text{test}} = 1.0$. All derivatives were computed using a first-order, three-point, centered difference approximation.

In Figure 6 we have plotted $\langle R \rangle$ and ΔR as the distance r_{test} from the centroid of the background field to the test charge is varied.

3.5. Separator Lengths

While $\langle R \rangle$ is the distance between the test charge and the closest field charge with which it shares flux, the length of the separator is related to the distance between these charges' nulls, A and B . Accordingly, we must modify this result to reflect test null-field null separation, instead of test charge-field charge separation. We account for the difference by adding the expected charge-null separation distances (see eq. [5]),

$$\Delta(r_{\text{test}}) = \sqrt{q_B/\bar{B}_r(r_{\text{test}})} \quad (19)$$

and

$$\Delta(r_{\text{test}} - \langle R \rangle) = \sqrt{q_B/\bar{B}_r(r_{\text{test}} - \langle R \rangle)}, \quad (20)$$

to $\langle R \rangle$. We denote this new quantity $\langle R_{AB} \rangle$,

$$\langle R_{AB} \rangle = \langle R \rangle + \Delta(r_{\text{test}} - \langle R \rangle) + \Delta(r_{\text{test}}). \quad (21)$$

To determine the standard deviation in the null-null distance from the charge-charge distance, we Taylor expand the expected field null-field charge separation from equation (5) to determine its dependence upon ΔR , which gives,

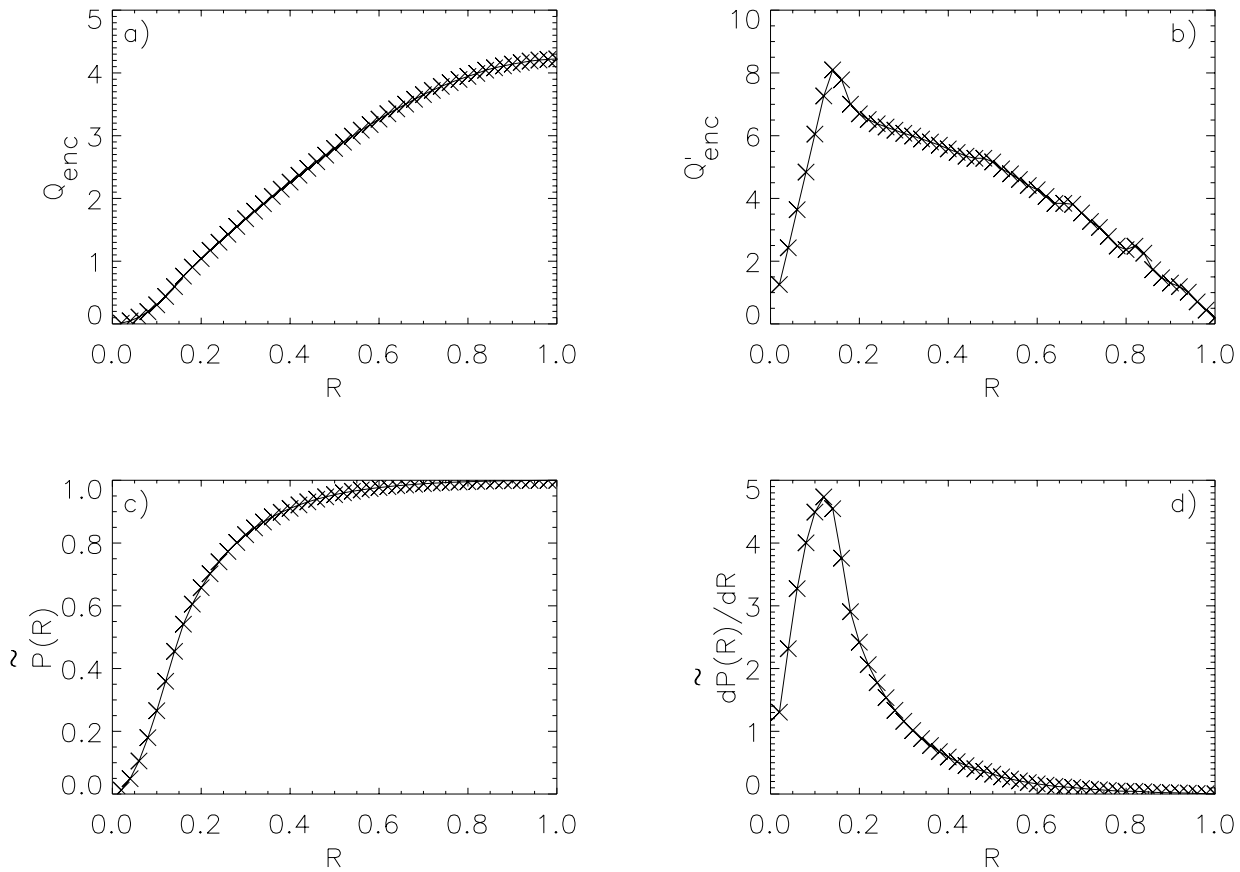


FIG. 5.—(a) $Q_{enc}(R)$, the vertical flux \bar{B}_z enclosed by \mathcal{C}_z within a distance R of the test charge, and (b) $dQ_{enc}(R)/dR$. (c) $\bar{P}(R)$, the probability that a field charge has been encountered within R of the test charge, given that \mathcal{C}_z encloses at least one field charge, and (d) $d\bar{P}(R)/dR$. All abscissae are in units of δ . Here $N = 100$ and $r_{test} = 1.0$.

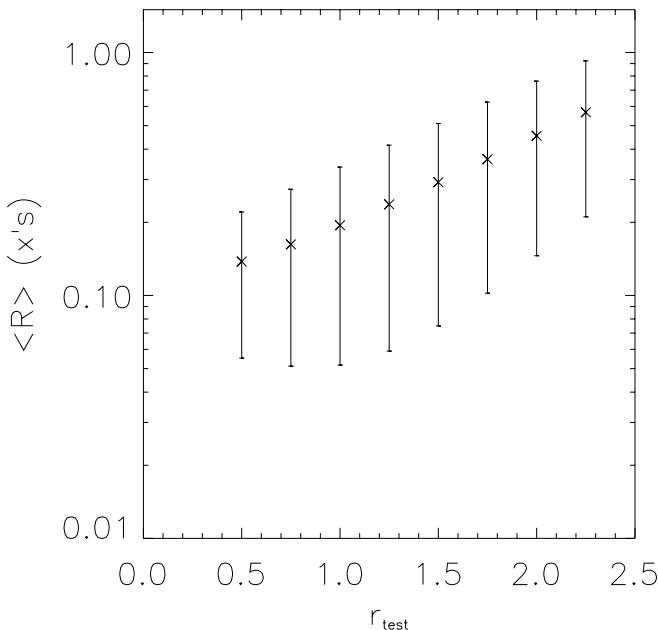


FIG. 6.—Plot of $\langle R \rangle$ and its standard deviation ΔR (vertical bars) as the distance r_{test} from the test charge to the centroid of the Gaussian background field is varied. Plot axes are in units of δ , and $N = 100$.

to first order in ΔR ,

$$\sqrt{q_B/\bar{B}_r[r_{test} - (\langle R \rangle \pm \Delta R)]} \approx \sqrt{q_B/\bar{B}_r(r_{test} - \langle R \rangle)} \left[1 \mp \frac{\bar{B}_r(r_{test} - \langle R \rangle)}{2\bar{B}_r(r_{test} - \langle R \rangle)} \Delta R \right]. \quad (22)$$

Since the background field is well behaved, we take $(\bar{B}_r/\bar{B}_r) \sim 1/\delta = 1$, implying that the variation in the null-charge distance is roughly half the standard deviation of the charge-charge distance. Accordingly, we approximate $\Delta R_{AB} = 1.5 \Delta R$. For comparison, we have plotted $\langle R \rangle$ and $\langle R_{AB} \rangle$ in Figure 7a as r_{test} is varied, with N kept constant at 100. The increase in $\langle R_{AB} \rangle$ for small r_{test} is an artifact of the symmetry in the background field: as $(r_{test} - \langle R \rangle)$ approaches zero, i.e., near the distribution's centroid, the radial field \bar{B}_r vanishes, which increases the field charge-field null distance, $[q_B/\bar{B}_r(r_{test} - \langle R \rangle)]^{1/2}$, added to $\langle R \rangle$ to get $\langle R_{AB} \rangle$.

Since these curves strongly suggest an exponential dependence on r_{test} , we fitted each to an exponential, using a nonlinear, least-squares χ^2 -minimization routine. The results of these fits are also shown in Figure 7a, with $\langle R \rangle = 0.084 \exp(0.85r_{test})$, and $\langle R_{AB} \rangle = 0.37 \exp(0.35r_{test})$.

We now make the simplifying assumption that the separator is a semicircular loop running through the

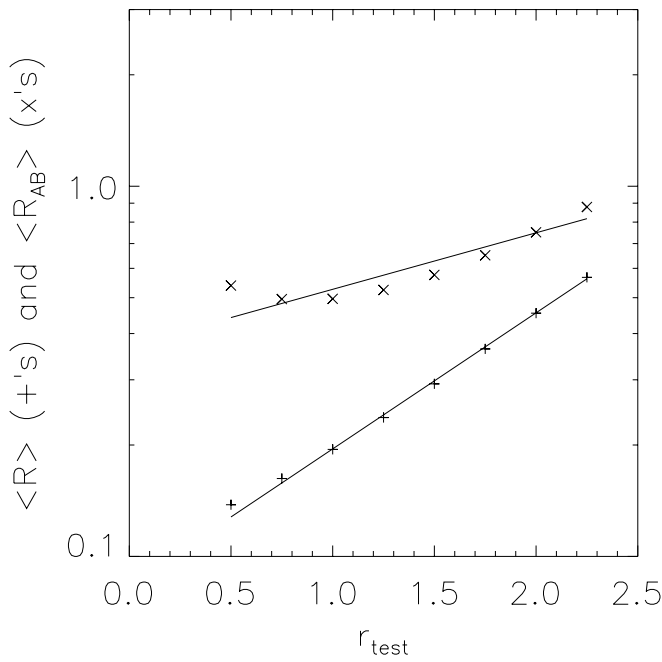


FIG. 7a

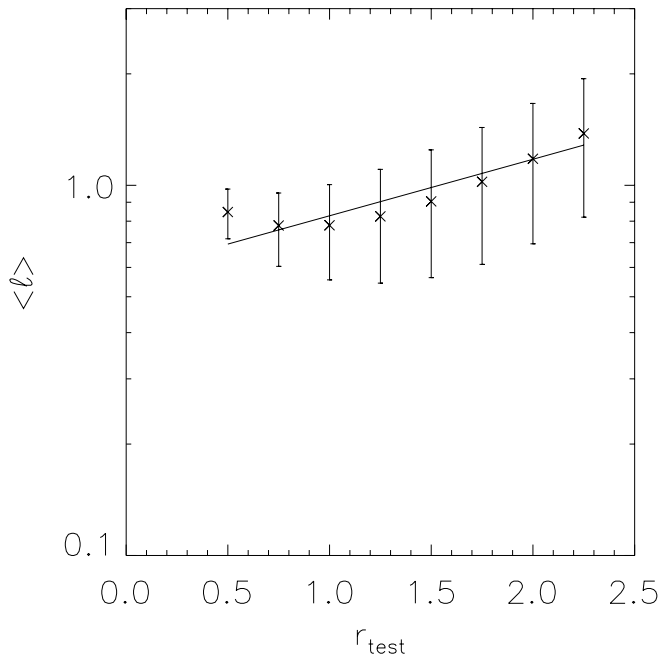


FIG. 7b

FIG. 7.—(a) Plot of $\langle R \rangle$ (plus signs) and $\langle R_{AB} \rangle$ (crosses), and exponential fits to each, as the distance between the test charge and background field's centroid, r_{test} , is varied. (b) A plot of $\langle l \rangle$ and Δl , with an exponential fit using $\langle l \rangle = \pi \langle R_{AB} \rangle / 2$, as r_{test} is varied. For both cases, plot axes are in units of δ and $N = 100$.

corona, in a plane perpendicular to the photosphere, from the field charge's null to the test charge's null. Hence, we can find the expected separator length $\langle l \rangle$ by multiplying the distance between the nulls, $\langle R_{AB} \rangle$, by $(\pi/2)$, which gives

$$\langle l \rangle = 0.58 \exp(0.35r_{\text{test}}). \quad (23)$$

In Figure 7b we show $\langle l \rangle$ and Δl , with a power-law fit, as r_{test} is varied.

In Figure 8a we show, on a log-log plot, $\langle l \rangle$ and Δl as the strength N of the background field, relative to that of the test charge, is varied, while r_{test} is held fixed at 1.5. A power-law fit of $\langle l \rangle$ as a function of N is also plotted. The χ^2 -minimization gives $\langle l \rangle = 7.0(N^{-0.45})$. A similar variation in $\langle l \rangle$ with N was observed for $r_{\text{test}} = 3$. As another rough approximation, then, $\langle l \rangle$ scales as $\sim 1/N^{1/2}$.

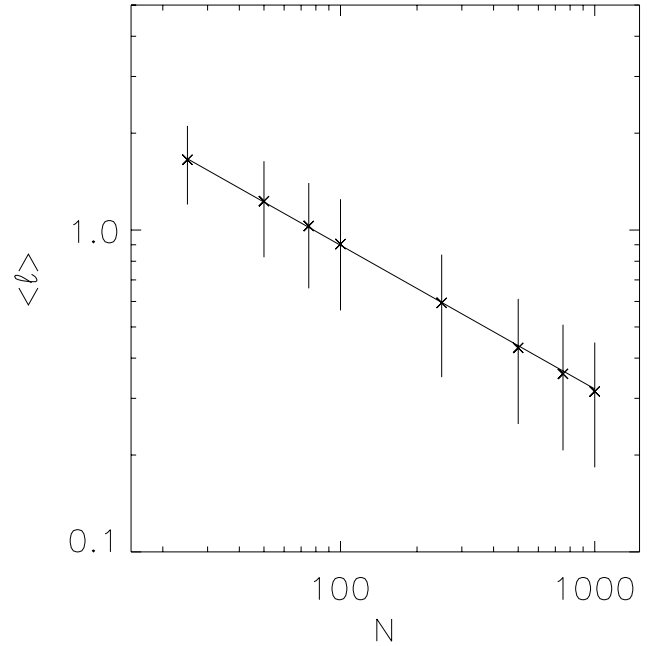


FIG. 8a

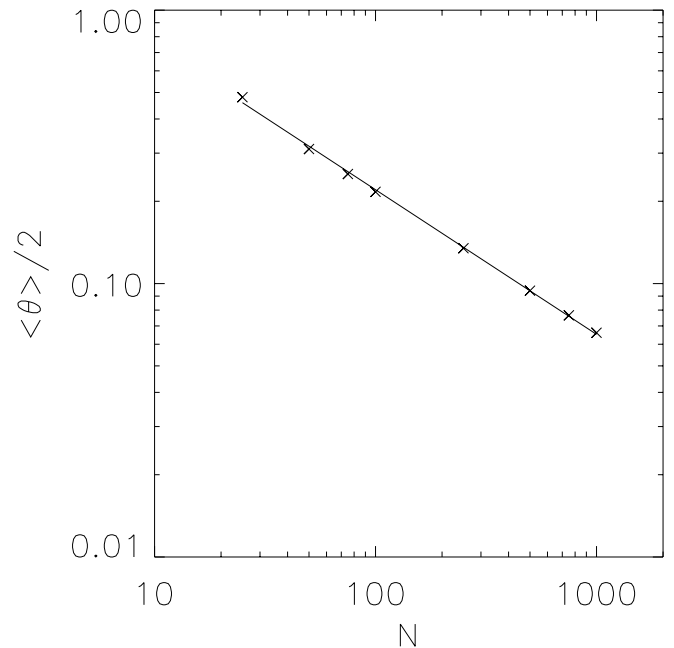


FIG. 8b

FIG. 8.—(a) Plot of $\langle l \rangle$ (crosses) and Δl as N is varied, and a power-law fit. The abscissa is in units of the test charge's flux, while the ordinate is in units of δ . (b) A plot of half of \mathcal{C}_x 's "opening angle" (see Fig. 4a), $\langle \theta \rangle / 2$ (crosses), and the χ^2 -minimization of a power-law fit, as background field strength, N , is varied. Here the abscissa is in units of the test charge's flux, while the ordinate is in radians. In both figures, r_{test} is held fixed at 1.5.

It should be emphasized that, since this entire development follows from finding the shortest distance to a field charge with which the test charge shares flux, $\langle l \rangle$ is the expected length of the *shortest* separator.

It is worth remarking that the “opening angle” of \mathcal{C}_Σ , defined as twice the inverse tangent of the slope of one of its “asymptotic” field lines (see Fig. 4a), exhibits a similar dependence: a fit of the half the opening angle, assuming a power law, gives

$$\langle \theta \rangle / 2 = 0.40(N^{-.53}), \quad (24)$$

as shown in Figure 8b. For large r_{test} , the opening angle is independent of r_{test} .

4. A MONTE CARLO TEST

To test the results of the mean-field scheme of the previous section, we now ignore the averaging used there and employ a distinct method of averaging here, working directly with fields that arise from a distribution of discrete flux elements.

We generate N random locations of field charges (x_i, y_i) , for $i = 1, 2, 3, \dots, N$, using normal deviates. Since results derived from a single realization of such a model active region are statistically meaningless, we study many realizations of such distributions—a Monte Carlo method—to find “ensemble averaged” quantities. In this way, we seek to confirm the mean-field approximation used in § 3.

4.1. Separatrix Rims with Discrete Charges

As a starting point, we consider the topological properties of such configurations. If all nulls are generic, then given $(N + 1)$ charges, there are N nulls, of which $(N - 1)$ are B -type and one is A -type. Since a separator must run from a B -type null to an A -type null, $N \geq 2$ is a necessary condition for a separator to exist. Since the existence of a separator further requires that a field charge’s separatrix intersect the test charge’s separatrix, a sufficient condition for the existence of a separator is that the test charge share flux with more than one field charge, which depends upon the details of a given configuration. To generalize, if the test charge shares flux with n of N field charges, there are only $(n - 1)$ separators; in every case, the flux shared between the test charge and exactly one of the field charges is not encircled by a separator. (In some configurations, more than one separator joined a given pair of nulls. When found, such configurations were not used in this work.)

Assuming the test charge shares flux with n of the configuration’s N field charges, we must find the lengths of $(n - 1)$ separators. From the definition of a separatrix, we know that all of the test charge’s field lines at $z = 0$ must lie along or within the separatrix rim \mathcal{C}_Σ (the intersection of the test charge’s separatrix and the photosphere). Hence, the n field charges and $(n - 1)$ nulls must lie on the boundary of, or within, the area enclosed by \mathcal{C}_Σ . This irregularly-shaped area has been termed the test charge’s “footprint.” In Figure 9 we show an example of a footprint. Notice the topological structure of \mathcal{C}_Σ : from the test charge’s A -type null, labeled A , two separatrix field lines run to field charges q_1 and q_4 ; from these charges, spines run to the field nulls B_{12} and B_{34} ; other spines run to these nulls from the field charges q_2 and q_3 ; finally, spines from these last two charges converge on the field null B_{23} .

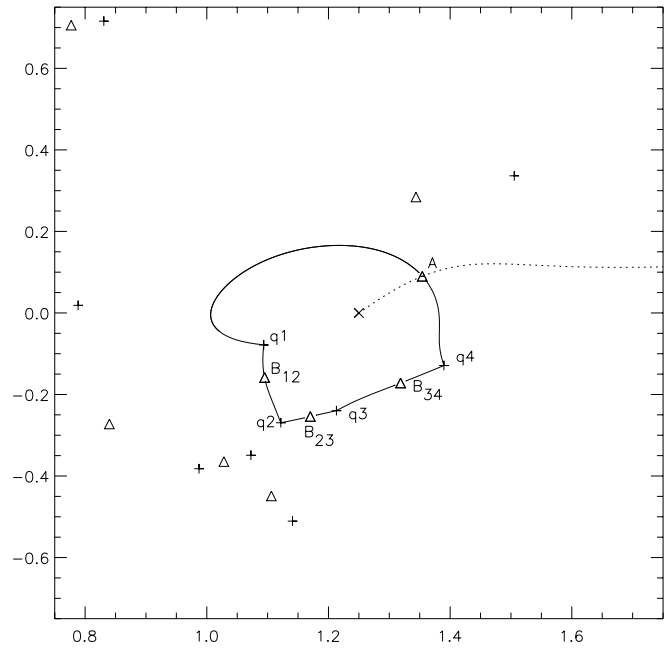


FIG. 9.—Test charge’s “footprint,” the area bounded by the separatrix rim, \mathcal{C}_Σ (the intersection of the test charge’s separatrix and the photosphere; solid line). Also shown are the A -type null’s two spines (dotted line): one runs from A to the test charge at the cross, while the other runs to $+\infty$. Here $r_{\text{test}} = 1.25\delta$ and $N = 100$.

4.2. Locating Nulls

As in the previous section, we assume that the separators are semicircular loops running through the corona from field null to test null. Since all nulls are assumed generic, the null associated with the test charge is the only A -type null in the configuration, which means all the separators have one end at this null. All of the B -type nulls at these separators’ opposite ends lie along or within \mathcal{C}_Σ . This means that we can find the separators’ lengths by finding the distance between the two nulls at each separator’s endpoints and multiplying the result by $\pi/2$.

Accordingly, we must determine the locations of the $(n - 1)$ B -type nulls associated with the n field charges that share flux with the test charge, as well as the location of the A -type null. Hence, we seek the locations of exactly n nulls. Finding the test charge’s null is straightforward, as its approximate location is known and its type is certain: Newton’s method in two dimensions suffices.

Locating the other $(n - 1)$ B -type nulls required more effort. The first method attempted involved finding all of the remaining $(N - 1)$ nulls using a two-dimensional Newton-Raphson routine. As we describe below, the convergence of Newton-Raphson depends on the initial guesses. It was found that not all of the nulls could be located this way using our initial guesses. (In configurations of $N = 100$ charges, only ~ 70 nulls were typically found within a few δ of the distribution’s centroid.)

A more successful technique focused on locating just the $(n - 1)$ nulls on or within the footprint, which are the only relevant nulls for our separator study. These B -type nulls were found from their relation to the n field charges in the footprint—the n field charges that share flux with the test charge. Field lines were integrated from the test charge to each of the field charges. From a starting point displaced

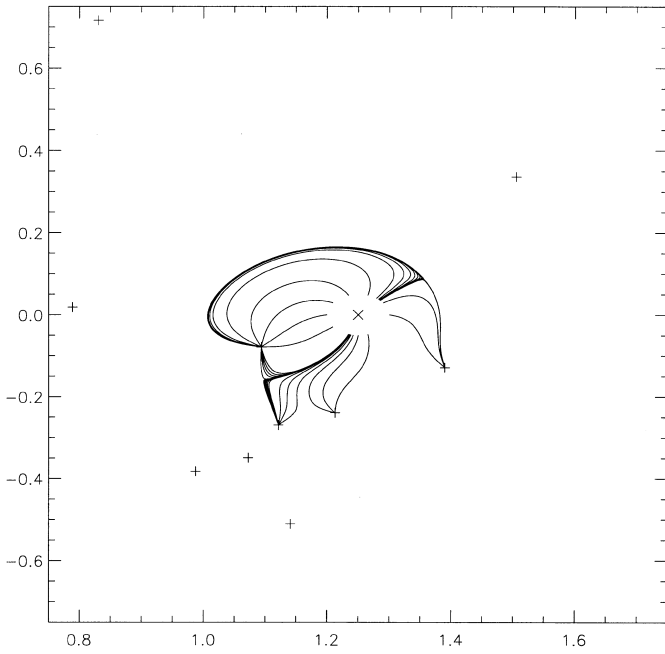


FIG. 10.—Plot of photospheric field lines (those at $z = 0$) that join the test charge to the field charges with which it shares flux. This footprint is the same as that in the previous figure.

from the test charge by a small distance Δr at an angle θ_1 , the field line was followed to its termination at field charge q_1 . This was repeated at angles θ_i , increasing by $\Delta\theta = 2\pi/10$, until a field line terminated at a different field charge q_2 . A field line was then traced from the angle $\theta' = \frac{1}{2}(\theta_{i-1} + \theta_i)$, bisecting the last interval. The terminus of this field line was used to refine the angular interval—a procedure repeated until the angular interval had been bisected 20 times, always bracketing q_1 and q_2 . This angular interval contains the

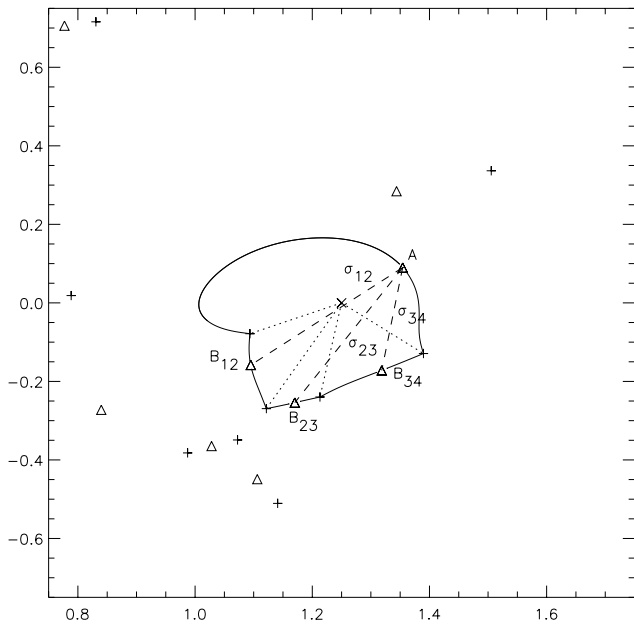


FIG. 11.—Plot showing the field null–test null distances (dashed line) used to find separator lengths. Also shown are field charge–test charge distances (dotted line). This is the same footprint appearing in the previous two figures.

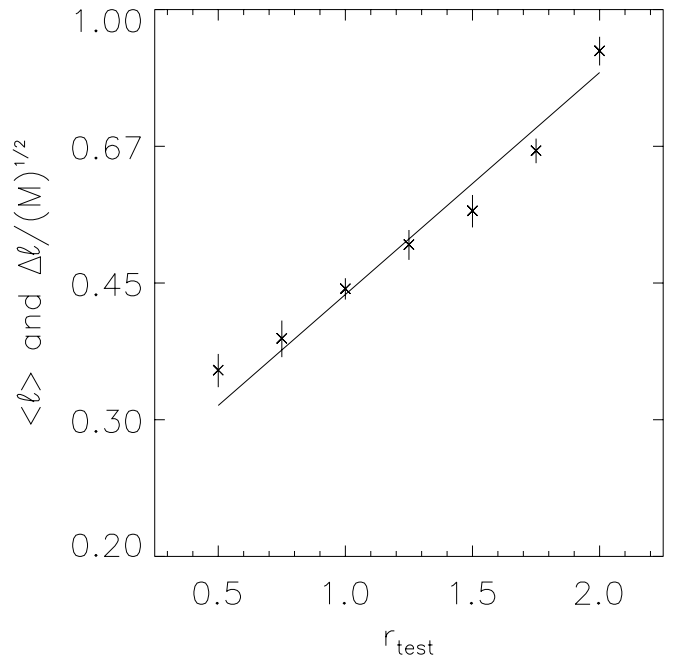


FIG. 12a

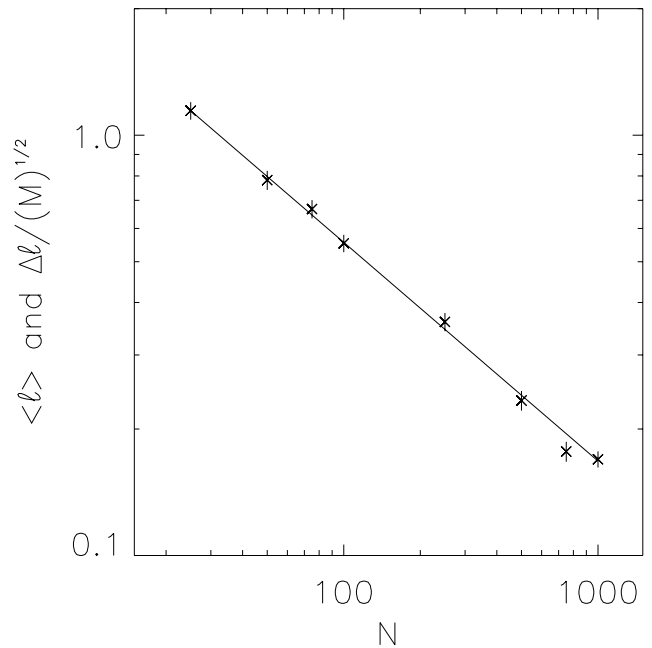


FIG. 12b

FIG. 12.—(a) Plot of the average shortest separator length, $\langle l \rangle$, and the standard error in the estimate, $\Delta l / M^{1/2}$, as r_{test} is varied. (M is the number of footprints studied.) An exponential fit is also plotted. N is fixed at 100 flux elements. Axes are in units of δ . (b) A plot of $\langle l \rangle$ and the standard error in the estimate as the number of charges in the background field, N , is varied, with r_{test} fixed at 1.5. A power-law fit to $\langle l \rangle$ as a function of N is also plotted.

separatrix dividing q_1 flux from q_2 flux. This separatrix must originate at a B -type null, which we label B_{12} .

Figure 10 shows the resulting photospheric field lines integrated from the test charge to the field charges with which it shares flux. This plot clearly displays the structure of that test charge's footprint as seen in Figure 9. Note the high density of integrated field lines near the separatrices

between field charges. We use the term “boundary lines” for the two integrated field lines closest to (but on opposite sides of) the separatrix of two given field charges.

The angular interval bracketing the separatrices can be used to locate the footprint’s field nulls. The nulls are located with the Newton-Raphson method. The most successful initial guesses proved to be:

1. The point midway between the pair of charges whose spines run into the null (without other charges, the null would be here).
2. The point at which the rate of growth in separation between the two boundary lines is greatest (near the null, boundary lines approach the null together, but leave in opposite directions).

In many cases, the null finder, fed an initial guess for a null’s location, does not converge to the null sought. One reason for this is that the field contains many more nulls than those on or within \mathcal{C}_Σ . Also, since the charge distributions are localized, the field is arbitrarily small far enough from the distribution, which means the null finder can find a field smaller than any threshold by running off to infinity.

To confirm that the null finder has indeed converged to the “correct” null from a given initial guess, one must integrate spines from the null which was found to verify that they run to “correct” pair of charges. If the null found is not associated with these charges, one must feed the null finder another guess and repeat the procedure.

Once the locations of all of the nulls in a given footprint are found, the distances between the *A*-type null and the *B*-type nulls are easily found, and, as discussed above, the result is multiplied by $(\pi/2)$ to yield the separator lengths.

For most choices of background field strength and test charge location, the null finder failed to find all the nulls in about 30% of cases. Unfortunately, the likelihood of such failures appears to be correlated with the number of field charges with which the test charge shares flux. Hence, as the density of background charges was increased, the failure rate increased as well. If all the correct nulls were not found, no statistics from that footprint were used in our calculations of separator lengths. This introduces a possible bias into our results for separator lengths: separators in footprints with more field charges might, on average, differ in length from those in footprints with fewer field charges, and we preferentially compile statistics from the latter.

Practically, however, since we are interested only in the length of the shortest separator, it is believed that the exclusion of footprints in which some of many nulls could not be found should negligibly affect our distribution of separator lengths.

4.3. Separator Lengths

For every test charge location and background field strength chosen, $M \geq 50$ “good” footprints were analyzed. A good footprint is one in which all nulls on or within \mathcal{C}_Σ were found, and all of these were of the correct type.

For each good footprint, the locations of all the nulls and their corresponding charges were stored. In addition to recording the total number of good footprints at a particular test charge location and background field strength, the number of cases in which nongeneric nulls were found and the number of cases in which not all nulls were found, i.e., failures, were also recorded.

By multiplying the shortest field null–test null distance (Fig. 11) by $(\pi/2)$, the shortest separator length for each footprint was found. Using all the footprints studied at each value of r_{test} and N , the average shortest separator length, $\langle l \rangle$, and its standard deviation, Δl , were then found.

In Figure 12a we show $\langle l \rangle$ as r_{test} is varied, as well as the standard error in the estimate, defined to be the standard deviation divided by the square root of the number of trials M , i.e., $\Delta l/M^{1/2}$. The number of background field flux elements, N , is held constant at 100. As in the mean-field case, it appears that $\langle l \rangle$ depends upon r_{test} exponentially. Here a χ^2 -minimization yields the result $\langle l \rangle = 0.22 \exp(0.65r_{\text{test}})$.

In Figure 12b we show, on a log-log plot, $\langle l \rangle$ and $\Delta l/M^{1/2}$ as the number of charges in the background field, N , is varied, while r_{test} is held fixed at 1.5. This plot suggests that, as in the mean-field case, $\langle l \rangle$ varies as some power of N . A χ^2 -minimization gives $\langle l \rangle = 6.1(N^{-.52})$. As in the mean-field case, then, $\langle l \rangle$ scales as $\sim 1/N^{1/2}$.

5. DISCUSSION

The goal of this work is to make statistical predictions of the lengths of coronal X-ray loops using a mean-field model of active regions, with simple parameters that can be used to characterize an active region—namely, physical size and net flux. It is also reasonable to expect that the length of such loops should depend upon their connectivity within the active region: loops with a footpoint at a flux element nearer the center of the active region, where the magnetic field geometry is more complex, are presumably shorter, on average, than loops on the fringes of the active region, where the magnetic features that share flux are farther apart. Simply put, since our hypothesis is that nulls form the footpoints of loops, and the density of nulls is lower where the density of charges is lower, loops should be longer when their footpoints are farther away from the distribution’s centroid.

To illuminate the dependence of loop lengths upon these parameters, we used the procedures outlined in §§ 3 and 4 to calculate the shortest separator length $\langle l \rangle$, and its standard deviation Δl , as a function of the location of the test charge relative to the background field’s centroid, and separately, as a function of the strength of the test charge relative to the total flux in the background field.

5.1. Comparisons

The two approaches outlined in the previous sections differ greatly in their underlying assumptions. We now compare the results obtained using the two methods. In Figure 13a we plot the expectation values for the lengths of the shortest separators, $\langle l \rangle$, and their standard deviations, obtained by the two methods discussed above, as r_{test} is varied. In Figure 13b we again plot the expectation values and standard deviations from both methods, this time as N is varied.

These results rather unambiguously tell us that separator lengths, as parameterized by N and r_{test} , have a functional dependence of the form

$$\langle l(r_{\text{test}}, N) \rangle = C\delta \frac{\exp(\alpha r_{\text{test}})}{\sqrt{N}}. \quad (25)$$

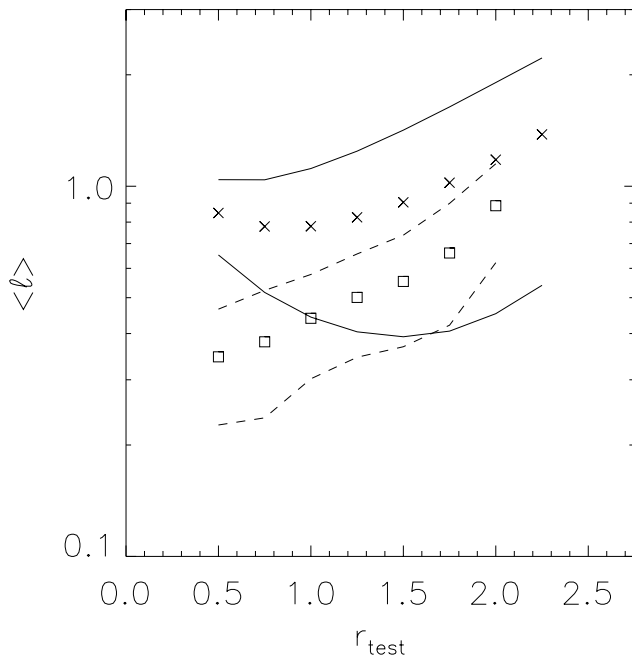


FIG. 13a

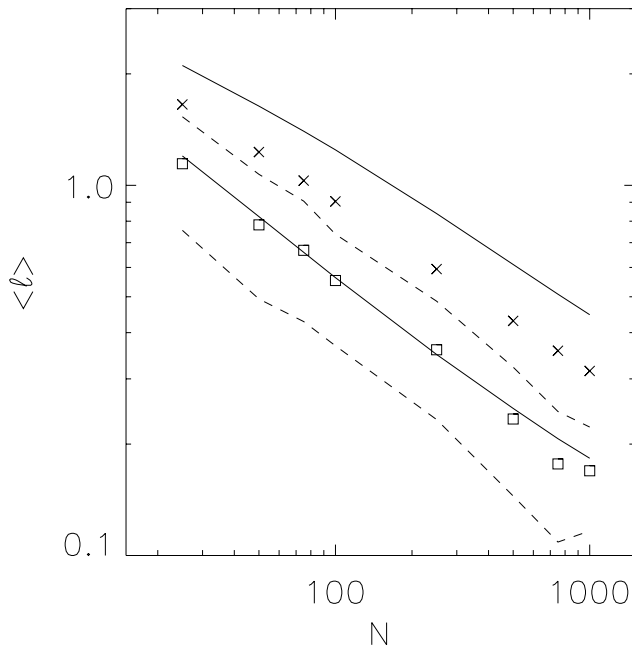


FIG. 13b

FIG. 13.—(a) Plot of $\langle l \rangle$ found by the mean-field (crosses) and Monte Carlo (open squares) approaches as r_{test} is varied. Intervals of 1σ are also plotted for each case mean field with solid and Monte Carlo with dashes. Axes are in units of δ ; N is 100. (b) A plot of $\langle l \rangle$ as the total flux in the background field is varied. Symbols/lines are as in previous plot. The abscissa is in units of the test charge's flux, while the ordinate is in units of δ . For this plot, $r_{\text{test}} = 1.5$.

Assuming $\alpha = \frac{2}{3}$, we find $C = 2.49$ (for $\alpha = .53$, we find $C = 3.06$). Therefore, we expect that loop lengths should decrease with either decreasing r_{test} or increasing N .

A comparison with the mean flux element separation

$$\lambda \equiv \sqrt{\frac{q_0}{\sigma}} = \delta \exp\left(\frac{r^2}{4\delta^2}\right) \frac{2\pi}{\sqrt{N}}, \quad (26)$$

where $\sigma = \overline{B_z}/2\pi$ is the surface “magnetic charge density,” shows that intuitive scaling relations are of limited utility in predicting separator lengths.

One thing is clear from these plots: both approaches lead to qualitatively similar results. What is less clear is the degree to which the two methodologies agree quantitatively. One way to investigate the quantitative agreement between the two approaches is to consider the distribution of separator lengths at a particular choice of r_{test} and N . For the mean-field case, the only pertinent result available is the differential probability distribution, $d\tilde{P}(R)/dR$ (see Fig. 5d); we interpret its peak to be the most likely charge separation. Thus, we cannot actually compare two distributions of test

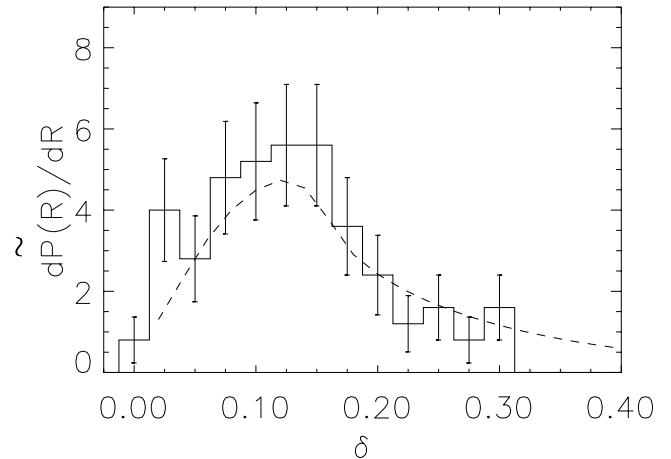


FIG. 14a

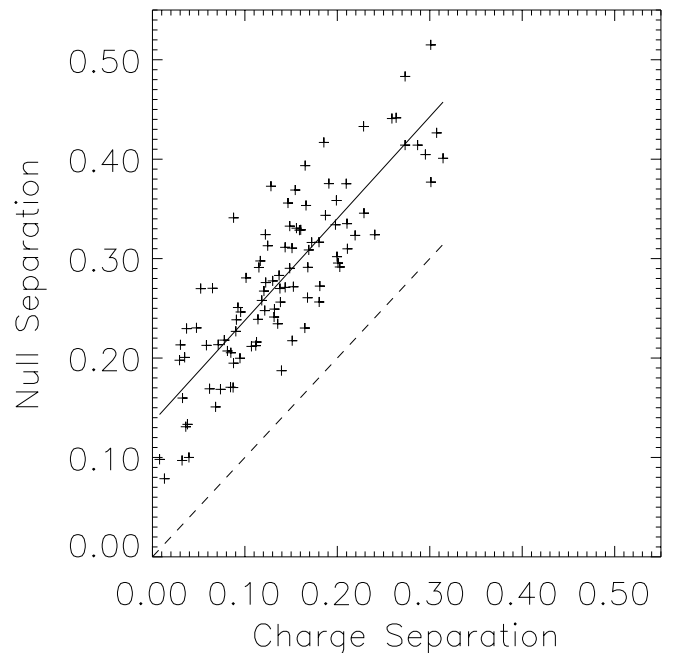


FIG. 14b

FIG. 14.—(a) Plot of $d\tilde{P}(R)/dR$ (dashed line), obtained with the mean-field approach, and a normalized histogram of charge separations, obtained with the Monte Carlo approach. (b) A scatter plot of charge and null separations, obtained with the Monte Carlo approach. A linear fit is plotted (solid line). Note that all null separations are longer than the charge separations, shown with a 45° line (dashed line). Clearly, charge separations and null separations are well correlated. Both abscissae are in units of δ , with $r_{\text{test}} = 1$ and $N = 100$.

null-field null separations. [To “convert” $d\tilde{P}(R)/dR$ into a distribution of null separations, while possible in principle, would introduce the nonlinearities seen in Fig. 7a.] Instead, we content ourselves with comparing $d\tilde{P}(R)/dR$ with the distribution of charge separations obtained with the Monte Carlo approach.

In Figure 14a we plot both a histogram of charge separations, obtained with the Monte Carlo approach, and the differential probability distribution for test charge-field charge separation, obtained with the mean-field approach. For the case shown, $r_{\text{test}} = 1$ and $N = 100$. To the extent that charge separations and null separations are well-correlated in the Monte Carlo case, this is a valid approach (see Fig. 14b).

This work demonstrates that a mean-field approach is both accurate, since it gives results in agreement with those from more detailed calculations, and powerful, in that it involves considerably less computational work than other methods.

5.2. Predictions

Several results from this work are noteworthy in that they can be observationally confirmed. Our test charge approach is most readily applicable to the case of a large unipolar distribution of magnetic flux in an active region, with very few isolated flux elements of minority polarity widely interspersed. In such a case, each member of the minority species is effectively a “test” charge, and the analysis presented above applies: δ is the core diameter of the unipolar distribution, the distance between the minority

element and the magnetic “center of gravity” of the active region is $r_{\text{test}}\delta$, and N is the ratio of majority flux to the flux in the minority element. We then expect the lengths of loops with a footpoint at the minority element to be given by equation (25).

In the conventional model of X-ray loops, it is assumed that such loops terminate in flux elements, or charges, of opposite polarity. In the separator model, however, X-ray loops end at null points of opposite type. As Figure 14b clearly illustrates, this work shows a significant difference in charge-charge and null-null separations. It is precisely these types of statistical differences between the two models that might allow observations to determine which model most accurately describes real X-ray loops.

As mentioned in the Introduction, Shimizu undertook a statistical survey of X-ray loops in SXT images and published a distribution of loop lengths (Shimizu et al. 1994). In Figure 14a we show a theoretical distribution of loop lengths, for a particular N and r_{test} . Unfortunately, this specification of N and r_{test} means that our results are not directly comparable to his. By both averaging such theoretical distributions over a suitable distribution of N and r_{test} , and by using more complex active-region models, we plan to generate more realistic distributions of loop lengths that can be compared with Shimizu’s.

This material is based upon work supported by the National Science Foundation under grant ATM 97-33424. The authors wish to thank A. Pevtsov for providing the image in Figure 1.

APPENDIX A

AVERAGE VERTICAL FIELD AT PHOTOSPHERE, \bar{B}_z

We have assumed a Gaussian probability distribution function for the field charge locations and now wish to derive an expression for the average vertical magnetic field at the photosphere. The \hat{z} -component of the discrete field (eq. [3]) there is given exactly by

$$B_z(x, y, 0) = q_0 \lim_{z \rightarrow 0} \sum_{i=1}^N \frac{z}{[(x - x'_i)^2 + (y - y'_i)^2 + z^2]^{3/2}}, \quad (\text{A1})$$

which is zero except at the charges’ locations, $(x, y, 0) = (x'_i, y'_i, 0)$, where it diverges. Now consider averaging over an infinite number of collections of N coordinate triplets $\{(x'_i, y'_i, 0)\}$, i.e., an ensemble of sets of charge locations,

$$\langle B_z(x, y, 0) \rangle = q_0 \sum_{i=1}^N \lim_{z \rightarrow 0} \left\langle \frac{z}{[(x - x'_i)^2 + (y - y'_i)^2 + z^2]^{3/2}} \right\rangle. \quad (\text{A2})$$

The average inside the sum can be written explicitly,

$$\lim_{z \rightarrow 0} \left\langle \frac{z}{[(x - x'_i)^2 + (y - y'_i)^2 + z^2]^{3/2}} \right\rangle = \lim_{z \rightarrow 0} \int_{-\infty}^{\infty} \int_{-\infty}^{\infty} \frac{z p_i(x'_i, y'_i) dx'_i dy'_i}{[(x - x'_i)^2 + (y - y'_i)^2 + z^2]^{3/2}}, \quad (\text{A3})$$

where each member $(x'_i, y'_i, 0)$ of each set $\{(x'_i, y'_i, 0)\}$ obeys the same probability distribution,

$$p_i(x'_i, y'_i) = \frac{1}{2\pi\delta^2} \exp \left[-\frac{(x'^2_i + y'^2_i)}{2\delta^2} \right], \quad (\text{A4})$$

as discussed above. Changing coordinates, $x_i = (x - x'_i)$, etc., and defining $r_i = (x_i^2 + y_i^2)^{1/2}$, the integrals for the i th charge become

$$\int \frac{z p_i(x'_i, y'_i) dx'_i dy'_i}{[(x - x'_i)^2 + (y - y'_i)^2 + z^2]^{3/2}} = \int_0^{2\pi} d\phi \int_0^{\infty} dr_i \left[\frac{z r_i}{(r_i^2 + z^2)^{3/2}} \right] p_i(x - x_i, y - y_i). \quad (\text{A5})$$

Next, we investigate the properties of the quantity in brackets in this equation, which we label $D(r_i, z)$:

$$D(r_i, z) \equiv \frac{zr_i}{(r_i^2 + z^2)^{3/2}}. \quad (\text{A6})$$

Integrating $D(r_i, z)$ over r_i on the interval $[0, \infty)$ gives unity,

$$\int_0^\infty \frac{zr_i dr_i}{(r_i^2 + z^2)^{3/2}} = \frac{-z}{(r_i^2 + z^2)^{1/2}} \Big|_0^\infty = 0 - \left(\frac{-z}{z} \right) = 1, \quad (\text{A7})$$

independent of z .

Observing that $D(0, z) = D(\infty, z) = 0$ we see that, as a function of r_i , $D(r_i, z)$ has a single maximum. Locating it by differentiating,

$$\frac{\partial D(r_i, z)}{\partial r_i} \Big|_{r_{\max}} = 0 = \frac{z}{[(r_{\max})^2 + z^2]^{3/2}} + \frac{3zr_{\max}^2}{[(r_{\max})^2 + z^2]^{5/2}} \quad (\text{A8})$$

$$0 = z^2 + r_{\max}^2 - 3r_{\max}^2 \quad (\text{A9})$$

$$r_{\max} = \frac{z}{\sqrt{2}}, \quad (\text{A10})$$

we see that, in the limit $z \rightarrow 0$, $r_{\max} \rightarrow 0$ as well. Further, since the height of the peak at r_{\max} ,

$$D_{\max} = D(r_{\max}, z) = D\left(\frac{z}{\sqrt{2}}, z\right) = \frac{2}{3\sqrt{3}} \frac{1}{z}, \quad (\text{A11})$$

is inversely proportional to z , in the limit $z \rightarrow 0$, D_{\max} diverges at r_{\max} . Finally, since the area under $D(r_i, z)$ when integrated over z is also unity, and $D_{\max} \propto z$, it must be the case that the width of the distribution, $\Delta D(r_i, z)$, scales directly with z ; hence, in the limit $z \rightarrow 0$, the peak also becomes infinitely sharp. Taken together, these facts imply that

$$\lim_{z \rightarrow 0} D(r_i, z) = \delta(r_i), \quad (\text{A12})$$

meaning that $\lim_{z \rightarrow 0} D(r_i, z)$ is a ‘‘one-sided’’ delta function. This makes evaluation of the integral in equation (A5) trivial,

$$\int_0^{2\pi} d\phi \int_0^\infty dr_i \delta(r_i) p_i(x - x_i, y - y_i) = 2\pi p_i(x, y). \quad (\text{A13})$$

Since $r_i = 0$ corresponds to $(x'_i, y'_i) = (x, y)$, the probability distribution we used in equation (A4) becomes

$$p_i(x, y) = \frac{1}{2\pi\delta^2} \exp\left[-\frac{(x^2 + y^2)}{2\delta^2}\right], \quad (\text{A14})$$

and we can finally write an expression for $\langle B_z(x, y, 0) \rangle$ in equation (A2),

$$\langle B_z(x, y, 0) \rangle = \frac{q_0}{\delta^2} \sum_{i=1}^N \exp\left[-\frac{(x^2 + y^2)}{2\delta^2}\right] \quad (\text{A15})$$

$$= \frac{q_0 N}{\delta^2} \exp\left[-\frac{(x^2 + y^2)}{2\delta^2}\right] \Rightarrow \quad (\text{A16})$$

$$\bar{B}_z(r) = \frac{q_0 N}{\delta^2} e^{-r^2/2\delta^2}, \quad (\text{A17})$$

where we have used $r^2 = x^2 + y^2$, and defined $\bar{B}_z(r) \equiv \langle B_z(r, 0) \rangle$. So both the average vertical field and the probability distribution of each set of charge locations are Gaussian.

APPENDIX B

AVERAGE RADIAL FIELD AT PHOTOSPHERE, \bar{B}_r

We now seek an analytic expression for the radial field at $z = 0$. Since the field is potential, $\mathbf{B} = -\nabla\chi$, finding $\chi(x, y, 0)$ amounts to finding $\mathbf{B}|_{z=0}$. Using \bar{B}_z from Appendix A, one can solve for χ by Fourier inversion, which gives

$$\chi(x, y, z) = q_0 N \int_0^\infty dk_r e^{-kr^2 \delta^2/2} J_0(k_r r) e^{-k_r z}, \quad (\text{B1})$$

where $r^2 = x^2 + y^2$. This integral, however, is analytically intractable.

Luckily, we seek the radial component of $\mathbf{B}|_{z=0}$, and

$$B_r \Big|_{z=0} = - \frac{\partial \chi}{\partial r} \Big|_{z=0} \quad (\text{B2})$$

$$= q_0 N \int_0^\infty dk_r k_r e^{-k_r^2 \delta^2/2} J_1(k_r r), \quad (\text{B3})$$

where we have employed the well-known relation $J'_0(k_r r) = -J_1(k_r r)$.

We then find

$$\begin{aligned} \bar{B}_r = B_r \Big|_{z=0} &= q_0 N \int_0^\infty dk_r k_r e^{-k_r^2 \delta^2/2} J_1(k_r r) \\ &= \sqrt{\frac{\pi}{2^3}} \frac{q_0 N}{\delta^2} \left(\frac{r}{\delta}\right) \exp\left(\frac{-r^2}{4\delta^2}\right) \left[I_0\left(\frac{r^2}{4\delta^2}\right) - I_1\left(\frac{r^2}{4\delta^2}\right) \right]. \end{aligned} \quad (\text{B4})$$

REFERENCES

- Baum, P. J., & Bratenahl, A. 1980, *Sol. Phys.*, 67, 245
 Caligari, P., Moreno-Insertis, F., & Schüssler, M. 1995, *ApJ*, 441, 886
 Canfield, R. C., & Metcalf, T. R. 1987, *ApJ*, 321, 586
 Cowley, S. W. H. 1973, *Radio Sci.*, 8, 903
 Démoulin, P., Hénoux, J., & Mandrini, C. 1994, *A&A*, 285, 1023
 D'Silva, S., & Choudhuri, A. R. 1993, *A&A*, 272, 621
 Fan, Y., Fisher, G. H., & McClymont, A. N. 1994, *ApJ*, 436, 907
 Gabriel, A. H. 1976, *Phil. Trans. R. Soc. London*, A281, 339
 Gary, D. E., Hartl, M. D., & Shimizu, T. 1997, *ApJ*, 477, 958
 Gold, T. 1964, in *Symposium on the Physics of Solar Flares*, ed. W. N. Hess (Greenbelt: NASA), 389
 Gold, T., & Hoyle, F. 1960, *MNRAS*, 120, 89
 Gorbachev, V. S., & Somov, B. V. 1988, *Sol. Phys.*, 117, 77
 Greene, J. M. 1988, *J. Geophys. Res.*, 93, 8583
 Lau, Y.-T. 1993, *Sol. Phys.*, 148, 301
 Lau, Y.-T., & Finn, J. M. 1990, *ApJ*, 350, 672
 Leighton, R. B. 1964, *ApJ*, 140, 1547
 Lin, R. P., Schwartz, R. A., Kane, S. R., Pelling, R. M., & Hurley, K. C. 1984, *ApJ*, 283, 421
 Longcope, D. W. 1996, *Sol. Phys.*, 169, 91
 ———, 1998, *ApJ*, 507, 433
 Longcope, D. W., & Cowley, S. C. 1996, *Phys. Plasmas*, 3, 2885
 Longcope, D. W., & Fisher, G. H. 1996, *ApJ*, 458, 380
 Parker, E. N. 1955, *ApJ*, 121, 491
 ———, 1983, *ApJ*, 264, 635
 Parnell, C. E., Priest, E. R., & Golub, L. 1994, *Sol. Phys.*, 151, 57
 Porter, J. B., Fontenella, J. M., & Simnett, G. M. 1995, *ApJ*, 438, 472
 Press, W. H., Flannery, B. P., Teukolsky, S. A., & Vetterling, W. T. 1988, *Numerical Recipes in C* (2d ed; Cambridge: Cambridge Univ. Press)
 Priest, E. R., & Forbes, T. G. 1989, *Sol. Phys.*, 119, 211
 ———, 1999, *Magnetic Reconnection* (Cambridge: Cambridge Univ. Press)
 Priest, E. R., Lonie, D. P., & Titov, V. 1996, *J. Plasma Phys.*, 56, 507
 Priest, E. R., & Titov, V. 1996, *Phil. Trans. R. Soc. London*, 354, 2951
 Shimizu, T. 1995, *PASJ*, 47, 251
 Shimizu, T., Tsuneta, S., Acton, L. W., Lemen, J. R., Ogawara, Y., & Uchida, Y. 1994, *ApJ*, 422, 906
 Shimizu, T., Tsuneta, S., Acton, L. W., Lemen, J. R., & Uchida, Y. 1992, *Proc. Astron. Soc. Japan*, 44, L147
 Somov, B. V. 1992, *Physical Processes in Solar Flares* (Dordrecht: Kluwer)
 Sweet, P. A. 1958, in *Electromagnetic Phenomena in Cosmical Physics*, ed. B. Lehnert (Cambridge: Cambridge Univ. Press), 123
 Van Hoven, G., et al. 1980, in *Solar Flares*, ed. P. A. Sturrock (Boulder: Colorado Associated Univ. Press), 17
 Yeh, T. 1976, *J. Geophys. Res.*, 81, 2140